FLUID GEOCHEMISTRY AND ITS IMPLICATIONS ON THE GENESIS OF HUANGSHADONG GEOTHERMAL SYSTEM - A GRANITE-HOSTED AREA IN SOUTHEAST CHINA

Jiao Tian

Institute of Geology and Geophysics, Chinese Academy of SciencesBeitucheng Western Road 19,
Chaoyang District, Beijing, 100029
CHINA
tianjiao375@163.com

ABSTRACT

The chemical compositions and isotopes content of non-thermal (lake and groundwater), geothermal water and dissolved gas from a granite-hosted geothermal system in Southeast China were investigated to delineate their origin, mixing, water-rock interaction and to construct a conceptual geohydrological model. The δ^2H and δ^{18}O isotope composition of the waters indicate meteoric origin without magmatic water or seawater inputs. Other volatiles indicate air and crustal predominant, with dissolved N_2 accounting for up to ~ 94% of the volatile gases, and ^{3}He/^{4}He and ^{4}He/^{20}Ne ratios indicate <5% of mantle-derived contribution. The infiltrated water appears to circulate to a depth of up to ~3.5 km. The chemical components in geothermal water are largely ascribed to the water-rock interactions in the granite reservoir. Leaching of Na, K, Cl, SO_4 and trace elements results in higher concentrations of those elements in geothermal waters than in non-thermal waters. Based on this difference, the mixing ratios between the deep geothermal fluid and the non-thermal waters infiltering the system at shallower depth and the chemical composition of the deep geothermal fluid were calculated. Based on these results and the application of geothermometry, the reservoir temperature of the deep geothermal fluid was estimated to be ~165°C, implying a medium-enthalpy geothermal system with a power density of 5 MW/km^2 and a crustal heat source associated with granite intrusives. This study provides insight into the formation mechanism of geothermal systems in SE China and provides constraints for further exploitation of geothermal energy in the area.

1. INTRODUCTION

Hot springs at the surface are considered to indicate low- to medium- to high-enthalpy geothermal fluids at depth and are signs of a potential geothermal prospect (Craig et al., 2013; Stober and Bucher, 2013). Such hot springs commonly occur along the SE coast of China, with temperatures reaching up to 100°C (Jiang et al., 2019; Chen, 1992). The area also hosts some of the early geothermal power plants in China including the first low-enthalpy geothermal power plant at Fengshun which was constructed in 1970 but eventually closed (Xia and Zhang, 2019). In view of the potential geothermal resources and a long history of direct use in the area, geothermal studies and explorations have continued in SE China in the search for medium to high-enthalpy geothermal resources. Also, full utilization of the potential of geothermal energy is increasingly expected for this region because economic and social activities are

intense along the southeast coast, and so is the demand for non-fossil fuel energy (He et al., 2017).

Huizhou, a city in eastern Guangdong Province (Figure 1a, b) has attracted increased interest as a potential geothermal prospect. Many questions are still unanswered including the origin of the fluid, maximum depth of circulation, fluid temperatures at depth, and the evolution of the fluids including mixing with non-thermal water along flow paths to the surface. Application of isotope and geochemical analysis techniques are not only low-cost but also efficient and reliable methods for assessing the characteristics of subsurface geothermal systems including estimation of reservoir temperatures, hydrothermal fluid composition and various geohydrological features including fluid sources, flow paths and mixing (Arnórsson, 2000; Aggarwal et al., 2000).

With the aim of constraining the evolution of the geothermal fluid in Huizhou geothermal field, we systematically sampled fluid discharging from shallow geothermal wells and analysed it for chemical and isotopic compositions. Based on mixing delineating, reservoir temperature calculations, together with constraints of the geothermal background obtained from geothermal volatiles, we estimate the chemical composition of the reservoir fluid and propose a conceptual model that incorporates origin and evolution of the hydrothermal fluid in the Huangshadong geothermal system.

2. GEOLOGICAL SETTING

Huangshadong is a famous spa resort in Huizhou, a city in the eastern Guangdong province, SE China (Figure 1a). The annual average temperature is ~25°C. The altitude in the Huangshadong village is between 40 m and 60 m so that the local boiling point reaches up to 100°C. The small village is surrounded by hills as high as 340 m and bordered by a lake called Huangshadong Reservoir to the east (Figure 1c). This area lies in the subtropical monsoon climate zone with an annual precipitation of >2200 mm.
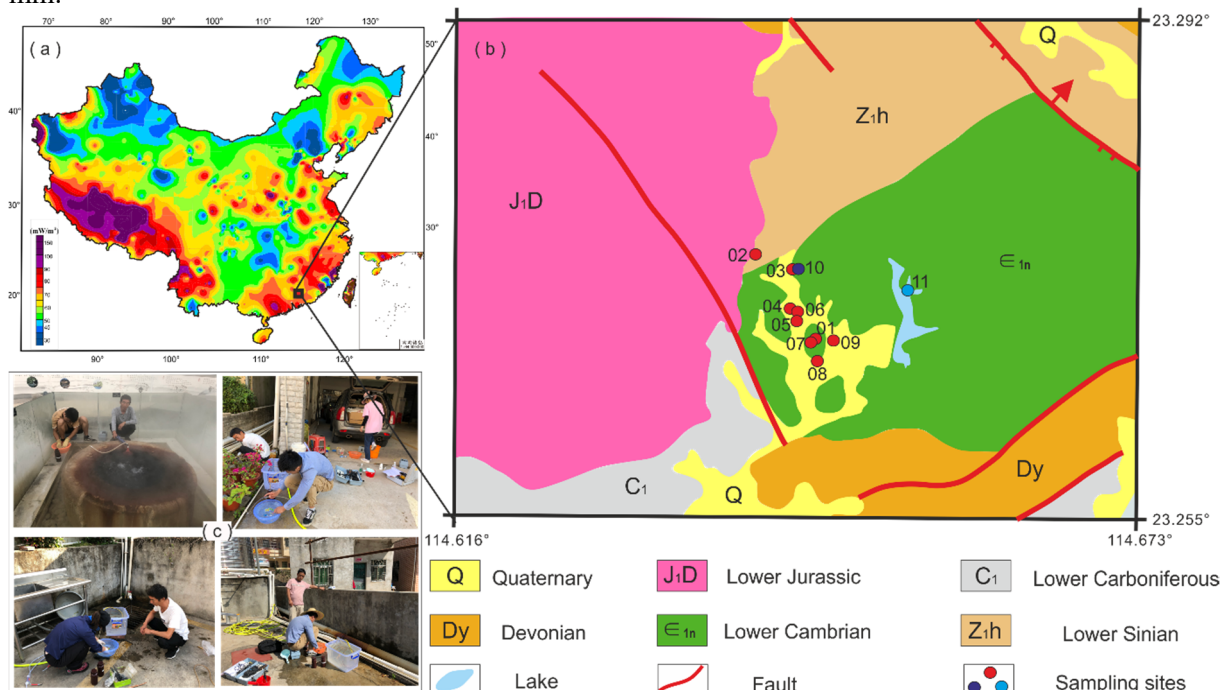

FIGURE 1: (a) Heat flow map of the continental China (Wang et al., 2012) and the location of the study area; (b) Simplified map of geological structure and the sampling sites in Huangshadong geothermal area. Solid circles of red, deep blue and light blue colour show the locations where samples of hot springs, groundwater and surface water were taken, respectively; (c) Photos of sampling

The study area belongs to the Wuyi-Yunkai Orogen in the Cathaysia Block (Li et al., 2019, Zhou and Li, 2000). The crust thickness is around 32 – 36 km (Leyla et al., 2015, Zhong and Zhou, 1990). The tectonic setting is mainly affected by the subduction of the Pacific plate and the Philippine Sea Plate under the Eurasian Plate, forming an intracontinental orogenic belt with a width of approximately 1300 km (Li, 2000, Li et al., 2012). Consequently, subduction-related tectonic thermal events occurred in this area igneous rocks are widespread, including granites and volcanic rocks from Triassic to Cretaceous (Li et al., 2012, Li et al., 2019). Studiy results show that the Late Mesozoic granites, which are also known as Yanshanian granite (ca. 175 – 140 Ma), were generated by remelting of Proterozoic crust (Li et al., 2007, Xiao et al., 2020). The age of the early Jurassic granite in Huangshadong geothermal field is 254 Ma (Kuang et al., 2020a).

As shown in Figure 1b, in Huizhou City, intrusive rocks are widely distributed and a series of NE-trending deep faults control the geological structure, including Fogang-Fengshun Fault, Heyuan Fault, Zijin-Boluo Fault, and Lianhuashan Fault. The Huangshadong geothermal field is in the Zijin-Boluo Fault zone and has exposed Early Jurassic Monzonitic granites. In addition, the sedimentary strata comprise Sinian sandstone, Cambrian feldspar quartz fine sandstone, Devonian coarse clastic rock, Carboniferous sandy shale coal interbed with seam, and Quaternary sand (Figure 1c) (Yan et al., 2019). The average value of the radiogenic heat rates of the Yanshanian granites in Huizhou is 6.7 $\mu W/m^3$ (Xiao et al., 2020). The radiogenic heat rate of the Jurassic granite mass is 3.15 – 5.78 $\mu W/m^3$, with an average value of 4.39 $\mu W/m^3$ (Kuang et al., 2020b).

3. SAMPLING AND METHODS

3.1 Water and gas sampling and analysis

Water samples from 9 geothermal wells, one groundwater well and one lake were collected as a part of this study. From the geothermal wells, 8 dissolved gas samples were collected at the same time. These wells were drilled by local people to source hot water for bathing except for the HZ02 well which is part of a geothermal park. The depth of the geothermal drilling holes ranges from 100 m to 400 m and the groundwater well is 25 m deep. The Huangshadong Reservoir is located to the east of the village.

Several parameters were analyzed on-site. Water temperature was measured at the well head with a handheld infrared thermometer. The pH, total dissolved solid (TDS), and electrical conductivity (EC) values were further measure on-site with a handheld multifunctional parameter measuring instrument, calibrated in the laboratory. The total alkalinity was also measured using the phenolphthalein and methyl orange titration method with a digital titrator and 0.41 mol/L H_2SO_4 and total S^{2-} and Fe^{2+} concentrations using a HACH DR-2800 spectrophotometer. Water samples for further chemical and isotope analysis were collected in high-density polyethylene bottles and filtered through 0.45 μm membranes. For anion, trace element and strontium isotopic analysis, reagent-quality HNO_3 (67%) was added to the samples to lower the pH below 2 (1 ml of acid per 100 ml sample). For SiO_2 analysis, the geothermal water was diluted twofold using deionized water to prevent precipitation of SiO_2. Samples for water isotope ($\delta\ ^2H$ and $\delta\ ^{18}O$) analysis were preserved in bottles without bubbles. All bottles were capped tightly and sealed with parafilm for storage.

Samples for dissolved gas analysis were collected with the gas drainage method in a lead glass bottle. To enhance the separation between geothermal water and gas, a copper cooling coil was connected to the wellhead. By submerging the cooling coil into a tank filled with cold water, the geothermal fluid degassed through the coil. After the gas had gathered in the glass bottle, the bottle was sealed with a rubber cap and encapsulated in a 500 mL polyethylene bottle which was filled with the raw geothermal water to avoid gas leakage (Tian et al., 2021). Three parrel samples were collected from each sampling site.

Major cations and trace elements were analyzed in the laboratory using ICP-OES and ICP-MS, respectively, whereas major anions were determined using IC. These were conducted at the Analytical

Laboratory of the Beijing Research Institute of Uranium Geology. The Sr isotopic composition was measured at the Isotope Organic Geochemistry Laboratory in the Institute of Geology and Geophysics, Chinese Academy of Science. Water isotopes ($\delta\,^2H$ and $\delta\,^{18}O$) were analysed in the Key Laboratory of Groundwater Resources and Environment in Jilin University, using a laser absorption water isotope spectrometer analyser. The analytical precision of $\delta^{18}O$ and δ^2H was 0.1‰ and 0.5‰, respectively. Gas samples were analysed in the Key Laboratory of Petroleum Resources Research, Northwest Institute of Eco-environment and Resources, Chinese Academy of Science. Gas compositions were determined using the mass spectrometer MAT 271 with relative standard deviations of less than 5%. The determination limit was 0.0001%. The measurement errors for carbon isotopic ratios were $\pm$ 0.2‰ and the analytical precisions of $\delta^{13}C$ values for both CO_2 and CH_4 was 0.3‰. The $^3He/^4He$ and $^4He/^{20}Ne$ ratios were determined with a Noblesse noble gas mass spectrometer (Nu Instruments, UK) calibrated with air from the Gaolan Hill area south of Lanzhou.

3.2 Geochemical calculations and geothermometers

Geochemical calculations performed in this study included aqueous speciation, mineral saturation (SI) and geothermometry calculations. The former calculations were conducted using the PHREEQC geochemistry program (Parkhurst and Appelo, 1999). For the geothermometry calculations, the chalcedony geothermometer, a Na-K-Mg triangular diagram, and the multiple mineral equilibrium approach were used to estimate the reservoir temperature. Furthermore, a silica-enthalpy warm spring mixing model, together with the analysis of the Na-K-Mg triangular diagram and chemical component compositions, was applied to delineate the mixing process occurring underground. The temperature equation for the chalcedony geothermometer was experimentally determined by Arnórsson et al. (1983). The Na-K-Mg triangular diagram is a simultaneous evaluation of water-rock equilibration conditions for the isochemical rock dissolution in geothermal reservoirs (Giggenbach, 1988). This diagram is derived from the combination of the K-Mg geothermometer and the Na-K geothermometer (Table 1), using thermodynamic data on K-feldspar, albite, and microcline to retrieve temperature equations. Based on the relative abundance of Na, K and Mg in water samples, Giggenbach (1988) classified them as "immature", "partially equilibrated or mixed" and "fully equilibrated". According to this method, the theoretical fully equilibrated ratios for Na/K and K/Mg can be calculated, and on this basis, the relative content in the reservoir fluid can be estimated. Therefore, theoretical mixing ratios can be estimated by assuming the composition of the other mixing endmember, e.g. surface water. The silica-enthalpy mixing model was initially developed for estimating subsurface temperatures in geothermal reservoirs. However, due to the variety in the enthalpy and solubility as the environment changes, this diagram provides additional information about the fluid's evolution upon rising to the surface.

TABLE 1: Geothermometer equations used in this study

Equation	Reference
$1112/(4.91 - \log S) - 273.15$	Arnórsson et al. (1983)
$\mathrm{Log}\,(Na/K) = -17.944 - 6427/T^2 + 2095.8/T$ $- 0.811 \times 10^{-6}T^2 + 5.482 \mathrm{Log} T$	Arnórsson et al. (1998)
$\mathrm{Log}(K^2/Mg) = -4410/T + 14.00$	Giggenbach (1988)

4. RESULTS

4.1 Major and trace element concentrations in water samples

The chemical composition of the water samples is reported in the APPENDIX table I. The water temperatures of geothermal well discharges ranged from 48°C to 55°C, except for well HZ02 which had water temperatures of 99°C. The HZ02 borehole also displayed the highest EC (1721 µs/cm) and TDS (727 mg/L). Other hot water samples exhibited relative low values for EC (479 – 1608 µs/cm) and TDS (192 – 633 mg/L), yet two orders of magnitude higher than those of the non-thermal water. All the

samples are characterized by neutral to slightly alkaline pH values (6.77 – 8.15). According to the major element systematics, the geothermal waters and groundwater are of Na·K-HCO$_3$ type, whereas the surface water is of NaCa-HCO$_3$SO$_4$ type (Figure 2). This indicates that Na and HCO$_3$ are the predominant ions in the geothermal waters whereas the concentrations of Cl, SO$_4$, K, Ca, and Mg are relatively low. Concentrations of SiO$_2$ in the geothermal waters vary from 33.7 mg/L to 186.9 mg/L.
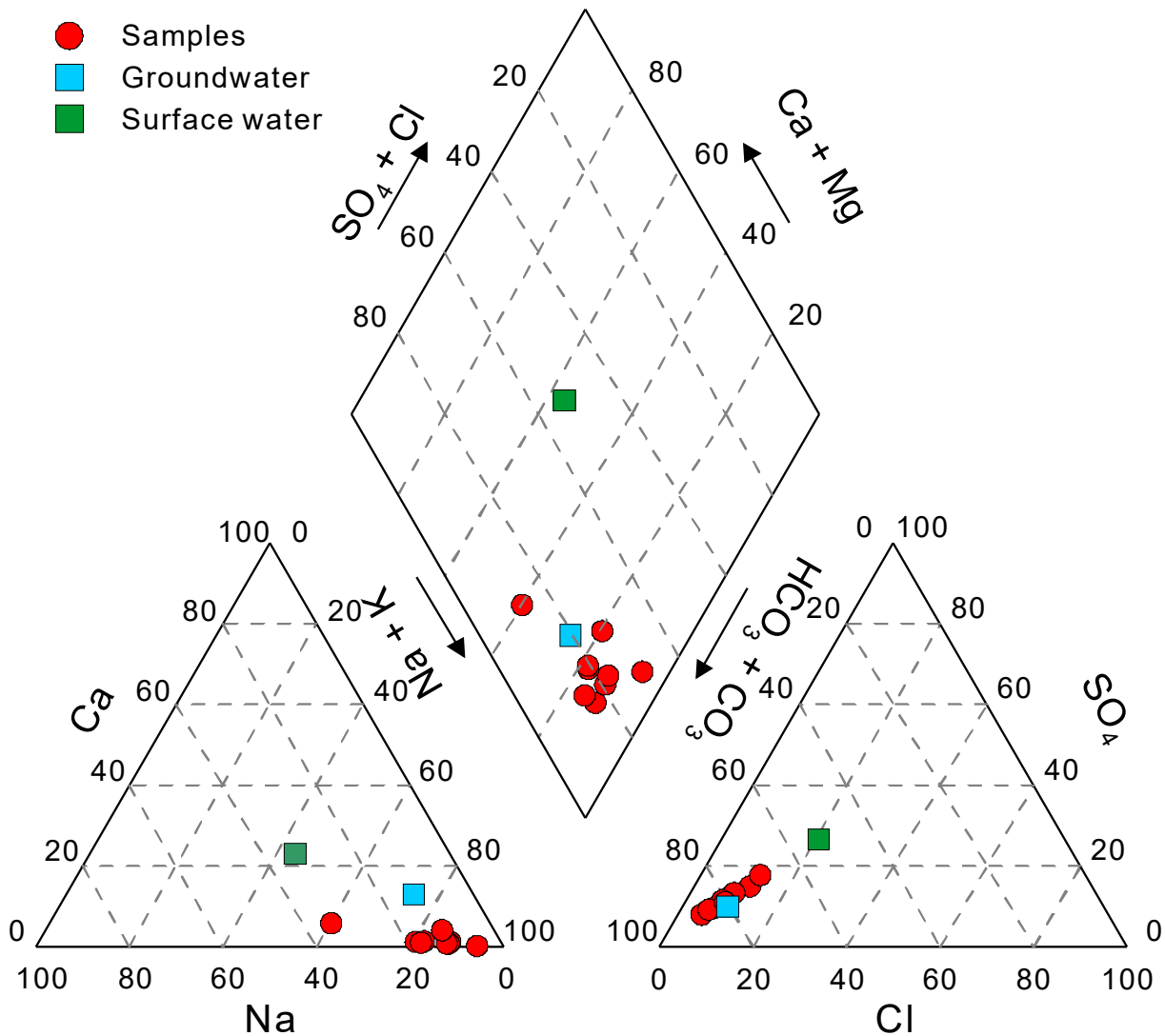

FIGURE 2: Piper diagram for water samples from Huangshadong geothermal field

The geothermal waters showed generally enriched concentrations of trace elements compared to the non-thermal surface water. Lithium (Li) was the most abundant trace element in the geothermal waters (1544 µg/L) and three orders of magnitude higher that in the non-thermal surface waters (1.2 µg/L). Similar enriched concentrations were observed for many other elements including Cs, W, S^{2-}, F, Br, Al, B, Be, Sc, Ti, Rb, Ba, Mn, and Sr, whereas other elements like Fe, As and Cy displayed similar concentrations in geothermal and non-thermal surface water. The highest concentrations of trace elements were generally observed for the water discharged by HZ02.

4.2 Dissolved gases

The results of the gas composition analysis are reported in the APPENDIX table II. The main gas observed is N$_2$, followed by variable amounts of O$_2$, CO$_2$, CH$_4$, Ar, He, and H$_2$. The content of N$_2$ varies

from the highest value of ~94.13 vol.% in HZ06 down to a value of ~76.81 vol.% in HZ07. The N_2 content does not correlate with venting temperatures but does inversely correlate with O_2 content. The air contamination could have occurred either during the sampling procedure or the determination process. CO_2 is the prominent non-atmospheric component and measured concentration lay within the range of ~0.89 – ~10.27%. In addition, concentrations of trace gases, He and H_2, vary in the range of ~0.05 – ~0.82% and 0.0003 – ~0.26%, respectively.

4.3 Isotopes

The stable oxygen ($\delta^{18}O$) and hydrogen (δ^2H) isotopic compositions of the waters range from -3.9‰ to -7.8‰ and from -28.6‰ to -46.0‰, respectively. The $^{87}Sr/^{86}Sr$ ratios of the geothermal water range from 0.7201 to 0.7338. The measured $^3He/^4He$ ratios range from 6.73×10^{-7} to 7.56×10^{-7}, which is equal to 0.48 Ra – 0.54 Ra. The $^4He/^{20}Ne$ ratios are in the range of 24 – 646, two to three orders of magnitude higher than the characteristic ratio of air which is 0.318 (Sano and Wakita, 1985).

5. DISCUSSION

5.1 Estimation of reservoir hydrothermal fluid composition applying geothermometry and mixing model

5.1.1 Geothermometry

Many chemical geothermometers have been developed to estimate subsurface geothermal temperatures, however, the Na-K-Mg triangle diagram is probably the most widely applied approach. It can be used to appraising the equilibrium status of geothermal waters as well as assessing mixing of non-thermal source waters with deep equilibrated geothermal reservoir water (Giggenbach, 1988). As shown in Figure 3, all the data points for the Huangshadong geothermal field, except for one, fall in the immature water zone in the Na-K-Mg plot. At the same time, these data points are distributed along a mixing line between the Mg-corner, corresponding to the surface water endmember, and the fully equilibrated point with a reservoir temperature of 165°C. This phenomenon suggests that the reservoir temperature of the study area is approximately165°C and that the chemical composition of surface discharges has been changed due to mixing with non-thermal water in the upflow zone. To delineate the mixing process between the reservoir fluid and surface water, we calculated the theoretically points for non-thermal water ratios from 10% to 95% in 5% intervals with subsurface temperatures of 150°C and 165°C, respectively. Thus, the mixing ratio for each sample could be estimated. For example, the geothermal water from HZ02 had the lowest mixing ratio of 45%. Other samples displayed much higher non-thermal water contributions of 65% to 95%. Moreover, the shift towards the lower temperature area indicates that a re-equilibration process is occurring due to the dilution effect. Meanwhile, the groundwater sample was estimated to contain approximate 5% of geothermal water. This result corresponds to other characteristics of the groundwater sample, such as the relative high temperature (32°C) and hydrochemical composition. Based on the reservoir temperature (165°C), the annual average temperature (25°C), and the regional geothermal gradient (40 °C/km), the circulation depth of the geothermal water can be calculated to be around 3.5 km.

Since the reservoir temperature is calculated to be lower than 180°C, chalcedony is the controlling mineral for silica dissolution (Arnorsson et al., 1983). According to the chalcedony equation shown in Table 1, the theoretical concentration of SiO_2 at reservoir temperature (165°) is calculated to be 236 mg/L. However, the maximum SiO_2 concentration in samples is 186.9 mg/L (HZ02) which corresponds to the theoretical value for a reservoir temperature of 150°C (191 mg/L), implying that dilution resulted from the mixing process.
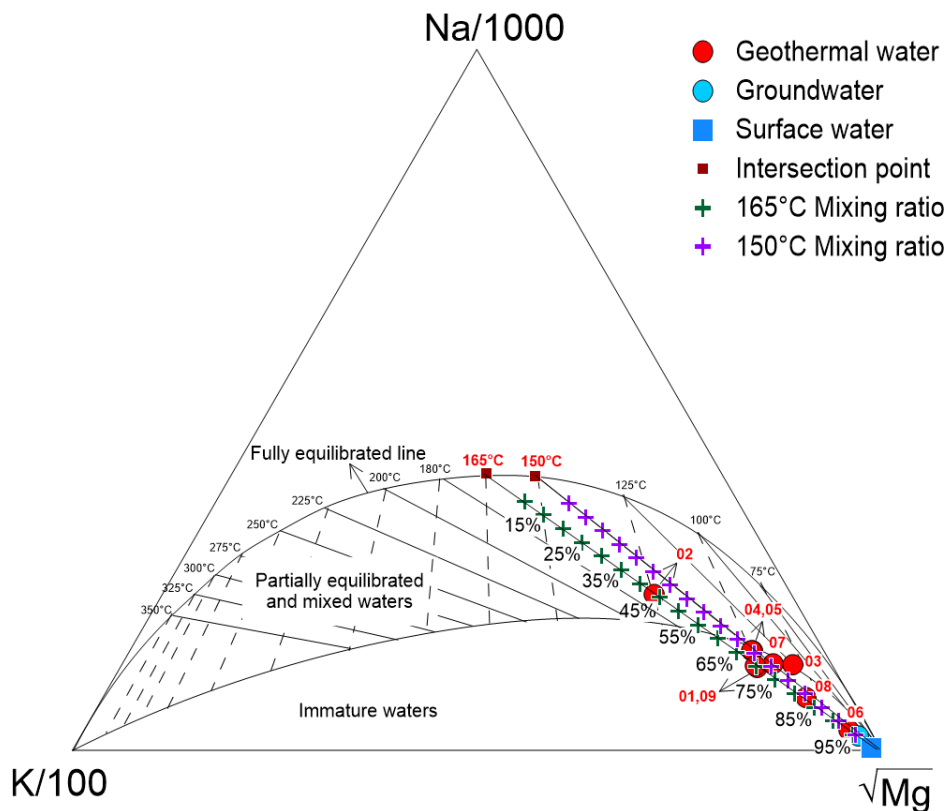
FIGURE 3: Na-K-Mg diagram and the calculated mixing ratios

5.1.2 Mixing model

Models have been developed to estimate the ratio of deep geothermal water in surface waters that have been mixed or diluted with non-thermal water (Arnórsson, 2000). In fact, mixing can be linked with parallel variations in the concentrations of non-reactive components in the water. Using the conservative components, linear relationships with Cl generally constitute good evidence for identifying and quantifying the mixing process. SiO_2 and Cl show a significant positive correlation with an R^2 value for the fit line of 0.87. Furthermore, concentrations of major components, such as K, Na, Ca, SO_4 and HCO_3, relate linearly with Cl concentrations with R^2 values > 0.9 (Figure 4). Simultaneously, many trace elements also show a linear relationship with Cl concentration, including F, Li, B, Br, Be, Sc, Ti, Cu, Rb, Cs, W, etc. These correlations suggest that these components are basically conservative in geothermal waters and that the geothermal waters discharging at the surface result of mixing of two endmembers. For most chemical components, the concentrations in reservoir fluid are higher than those in the cold-water endmember. This could be attributed to the fact that geothermal water tends to dissolve solids during the deep circulation underground and mixing is referred to as dilution.

5.1.3 Estimation of reservoir fluid composition

The concentrations of non-reactive components in mixed waters are determined by their content in the hot and cold-water components in the mixture and their relative proportions. According to the equation of the fitting line describing the correlation between SiO_2 and Cl (Figure 4), the theoretical concentration of Cl in the reservoir fluid is 79.3 mg/L and the theoretical concentration of SiO_2 is 236 mg/L at 165°C.
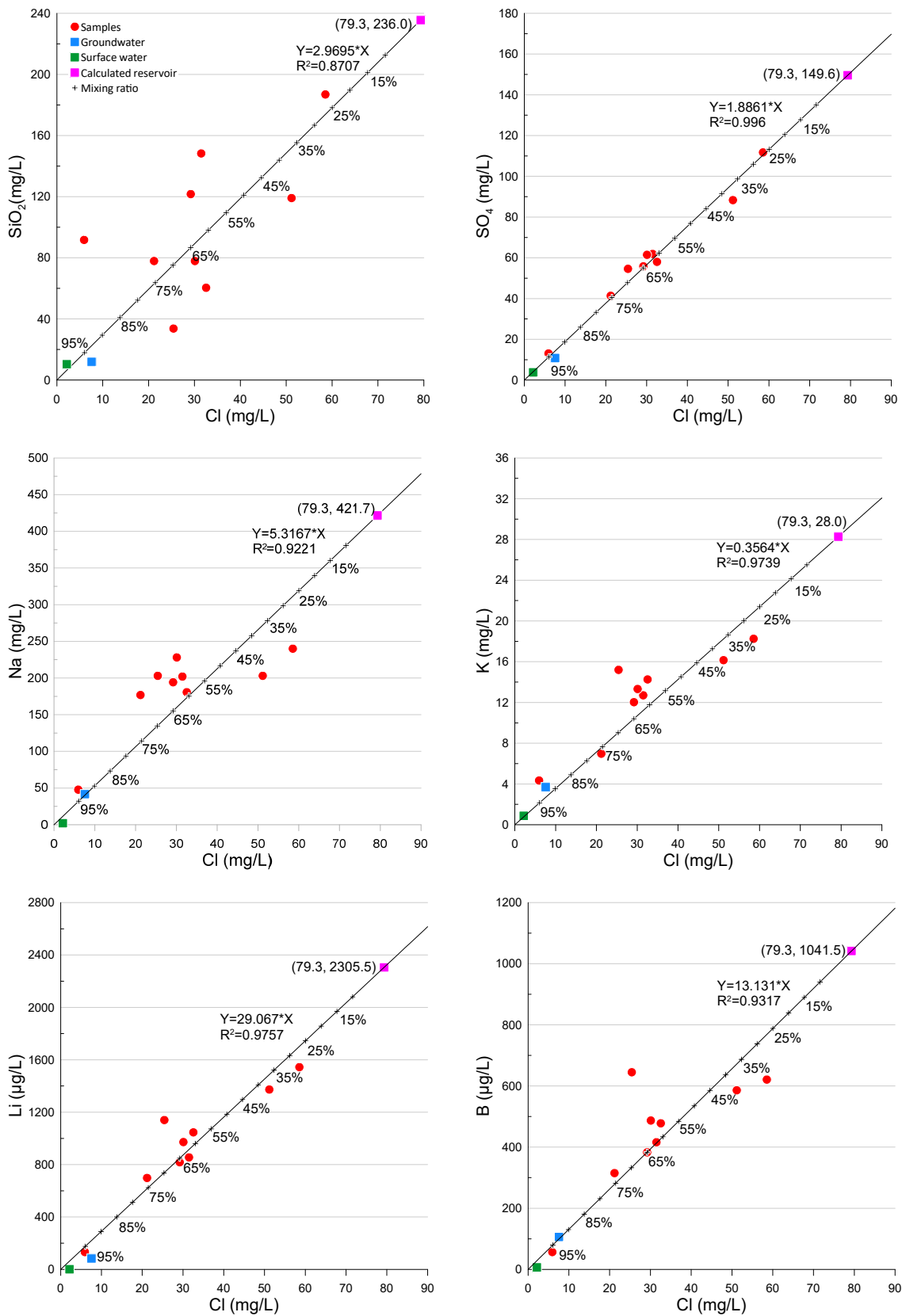
FIGURE 4: Mixing trend and mixing ratios derived for SiO_2, SO_4, Na, K, Li, and B versus Cl

Consequently, theoretical concentrations of other components in the reservoir can be calculated based on the theoretical Cl concentration (79.3 mg/L) and the equations for the respective mixing trend. All

the calculated results are shown in the plots as the geothermal endmember. For example, the calculated concentrations of K, Na, Ca, Mg, SO_4, HCO_3, F, Li, B, Br and Rb are 28.0 mg/L, 421.7 mg/L, 73.9 mg/L, 0.3 mg/L, 149.6 mg/L, 1070.9 mg/L, 21.0 mg/L, 2305.5 µg/L, 1041.5 µg/L, 146.5 µg/L and 392.0 µg/L, respectively. Based on the chemical composition, the pH value and total alkalinity were calculated using the PHREEQC program. The values are 7.6 and 0.017 eq/kg, respectively. As shown in Figure 5, the log (Q/K) values (mineral saturation state) tightly converged at ~150 – 165 °C. Furthermore, assuming the surface water as the cold-water endmember, mixing ratios for each component, except for Mg, can be calculated. For HZ02, which has the highest content of Cl, the mixing ratios of cold water vary from 25 % – 45%. Most other samples exhibit ratios around 55% – 75%. These results correspond to those from the Na-K-Mg triangle diagram in Figure 3.
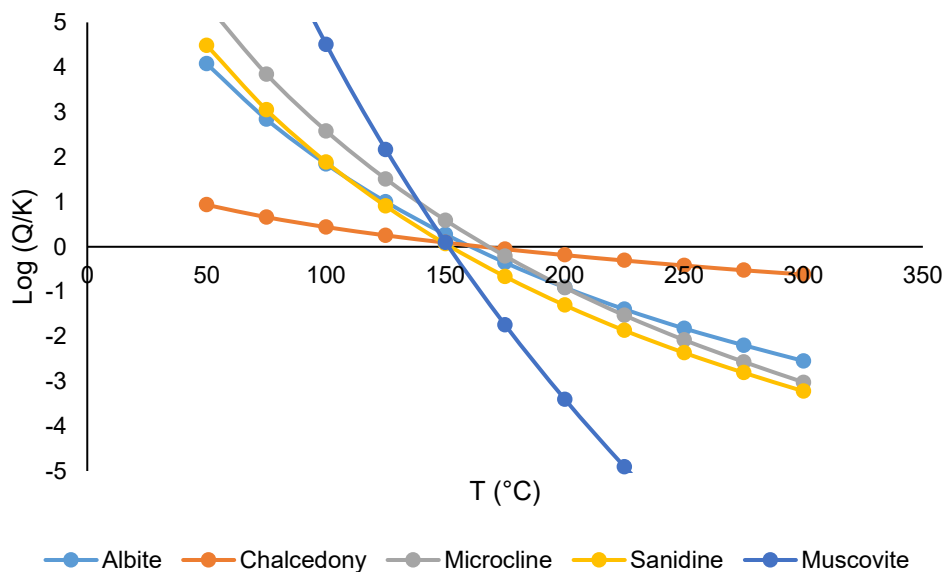

FIGURE 5: Log (Q/K) versus temperature for calculated reservoir fluid

5.2 Water and volatile element origin

5.2.1 Origin of hydrochemical compositions

The results for the $\delta^{18}O$ and δ^2H concentration closely correspond to the meteoric water line, suggesting their meteoric origin (Figure 6). However, the positive $\delta^{18}O$ shift which could result from high temperatures or long-term water-rock interaction in geothermal systems that cannot be recognized in this plot. This phenomenon indicates that neither typical high-temperature geothermal water, nor old geothermal water is likely to be present in the Guanzhong sedimentary basin (Li et al., 2017) and are not expected in the study area. Located near the Local Meteoric Water Line (LMWL), the groundwater is also recharged by infiltrated precipitation, whereas the location where the lake sample was taken shifts towards the right of the LMWL due to the evaporation effect (Pang et al., 2017). It is apparent that the $\delta^{18}O$ and δ^2H values of geothermal water are more depleted than those of the surface water and the groundwater. According to the elevation effect of water isotopes, the recharge elevation is higher than those of the groundwater and the surface water.

Since the origin of geothermal water is infiltrated precipitation without other sources, such as seawater or magmatic water, the hydrochemical components largely come from dissolution of rock minerals and gases. According to the multiple mineral equilibrium simulation shown in Figure 5, albite ($NaAlSi_3O_8$), chalcedony (SiO_2), microcline ($KAlSi_3O_8$) and sanidine ($KAlSi_3O_8$) are the major minerals controlling the aqueous chemical equilibrium. Thus, the dominant cations in geothermal water, Na and K, mainly come from the water-rock interaction between infiltrated precipitation and granites. This is confirmed by the thermodynamic activity plots of the $Na_2O-Al_2O_3-SiO_2-H_2O$ system and the $K_2O-Al_2O_3-SiO_2-H_2O$ system in Figure 7. The data points for the calculated reservoir fluid fall within the field of albite for the

Na system, and in the microcline field for the K system. Moreover, their locations are in the areas bounded by the lines for 100 °C and 200 °C, confirming that the equilibrium temperature is in this range. The chemical reactions between water, dissolved carbon dioxide and reservoir rocks containing albite and microcline as major minerals (Eq. 1 and 2) control and dictate the composition of the alkaline HCO_3-Na type geothermal fluid.

$$2NaAlSi_3O_8 + 9H_2O + 2H_2CO_3 \rightarrow Al_2Si_2O_5(OH)_4 + 4H_4SiO_4 + 2Na^+ + 2HCO_3^- \qquad (1)$$

$$2KAlSi_3O_8 + 3H_2O + 2CO_2 \rightarrow Al_2(Si_2O_5)(OH)_4 + 4SiO_2 + 2K^+ + 2HCO_3^- \qquad (2)$$
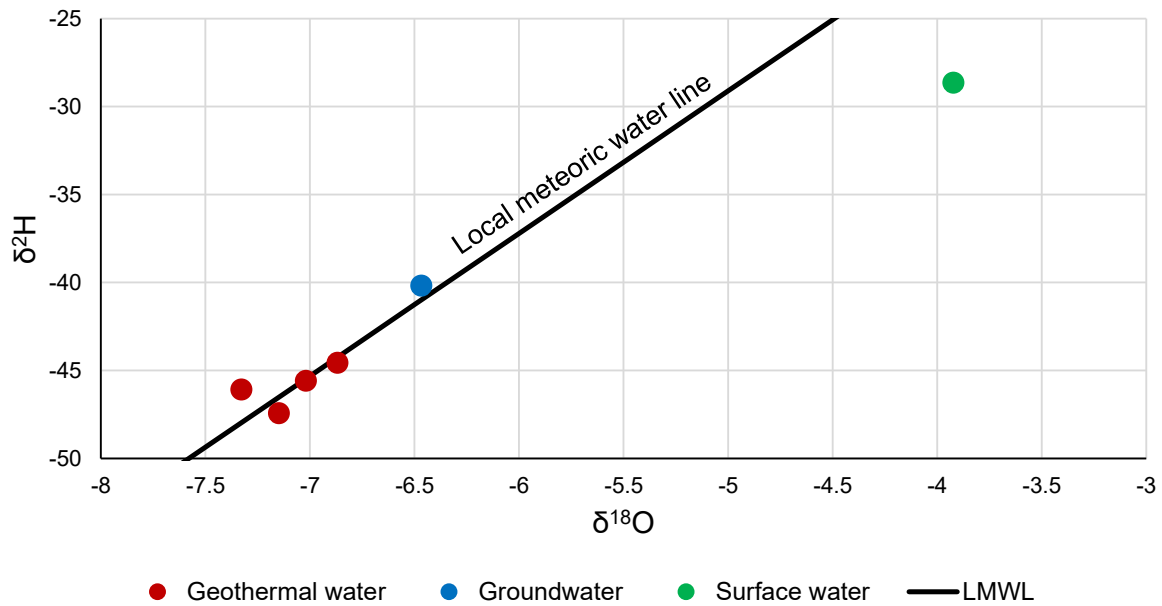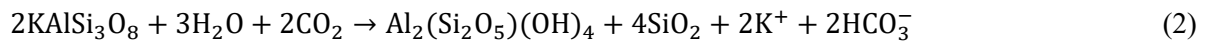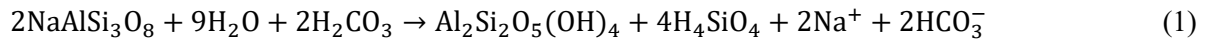
FIGURE 6: Plot of $\delta^{18}O$ and δ^2H values of water samples in this study
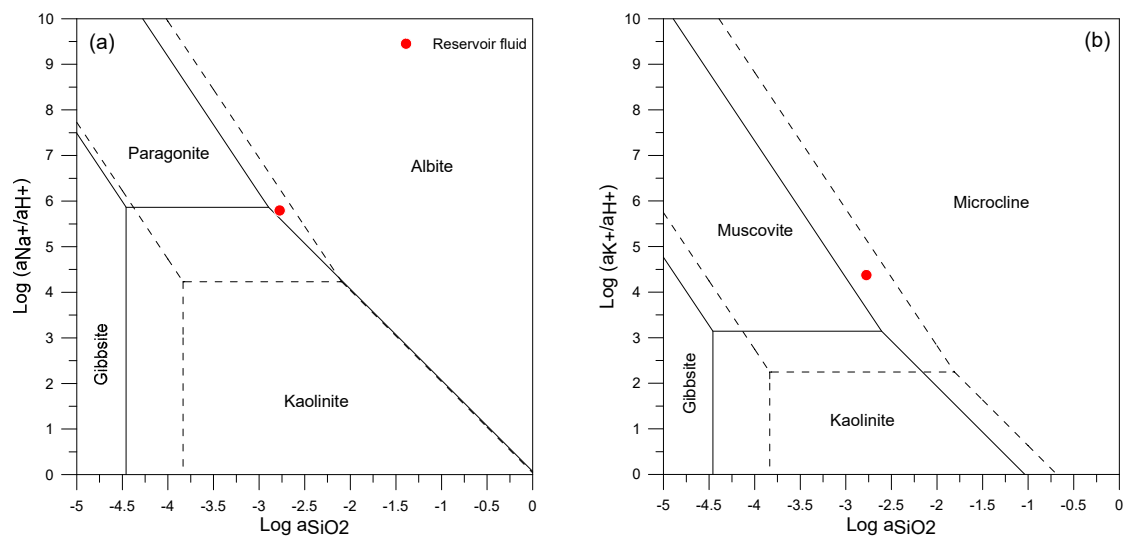
FIGURE 7: Thermodynamic activity plots of (a) the Na_2O-Al_2O_3-SiO_2-H_2O system and (b) the K_2O-Al_2O_3-SiO_2-H_2O system at 100 °C (solid line) and 200 °C (dashed line). The activity values of Na, K and SiO_2 were calculated by the PHREEQC input file used in section 5.1.

Accumulation of trace elements in geothermal waters exhibits the chemical characteristics of reservoir rocks. As previously mentioned, the concentrations of geothermal suite, Li, B and F, in the study area are enriched thousands to hundreds of times compared to those in local surface water. Simultaneously,

they exhibit a linear correlation with Cl concentrations, suggesting their common source in the strata. According to the geological setting, the water-rock interaction between water and the underlying granite could result in such hydrochemical compositions. Lithium could leach from biotite, feldspar, and plagioclase in granite (Zhang et al., 2021). Boron tends to come from amphibole, biotite, plagioclase and felspar (Leeman and Sisson, 1996, Zhao et al., 2011). Fluoride is possibly originating from dissolution of biotite and fluorite (Chevychelov et al., 2008). All these minerals are typical rock-forming minerals of granite (Huang et al., 2013, Zhu et al., 2010) and the fluorine composition for biotite from Guandong Jurassic granite reaches up to 0.75 wt% (Huang et al., 2013). Sr concentrations in geothermal water are two orders of magnitude higher than in surface water, indicating enrichment during the water-rock interaction. However, all the water samples have similar $^{87}Sr/^{86}Sr$ ratios in a range of 0.7201 – 0.7338, close to the characteristic $^{87}Sr/^{86}Sr$ ratio for granite (0.724) and syenite (0.718 – 0.723) (Riishuus et al., 2003, Shand et al., 2009). Thus, the isotopic ratios of both geothermal and surface waters could be due to the underlying Cambrian feldspar quartz fine sandstone (Figure 1c). In addition, the $^{87}Sr/^{86}Sr$ ratio of a granite pluton in Boluo County of Huizhou, 50 km to the west of the study area, was reported to be 0.7354 (Ling et al., 2006), implying a possible effect of the Jurassic Monzonitic granite. Furthermore, the correlation matrix (the APPENDIX table VI) of ionic concentrations shows strong correlations of these ions with not only the major ions, such as Na, K, Cl, SO$_4$, but also other trace elements, including Br, Be, Sc, Ti, Rb, Cs, W, etc., indicating that they originate from the same granitic reservoir.

In addition, the APPENDIX table III lists rare earth element (REE) concentrations in the water samples and the δCe and δEu values which indicate Ce and Eu anomalies. North American Shale Composite (NASC) (Taylor and Mclennan, 1985) normalized REE distribution patterns of water samples are shown Figure 8. The REE patterns vary little among the geothermal waters and are consistently depleted of the light rare earth elements (LREE) but are enriched in the heavy rare earth elements (HREE). All samples exhibit a positive Eu anomaly (δEu: 1.31 – 13.16) which suggests affinity to feldspar-containing minerals in the reservoir rocks (Liu et al., 2016). Moreover, the slight alkaline environment could result in the release of HREEs into geothermal water but the reabsorption of the LREEs into the solid particles (Byrne and Kim, 1990, Dupré et al., 1996). In addition, the REE patterns of the geothermal waters are quite different from those of the groundwater and surface waters, indicating different water-rock interaction processes.
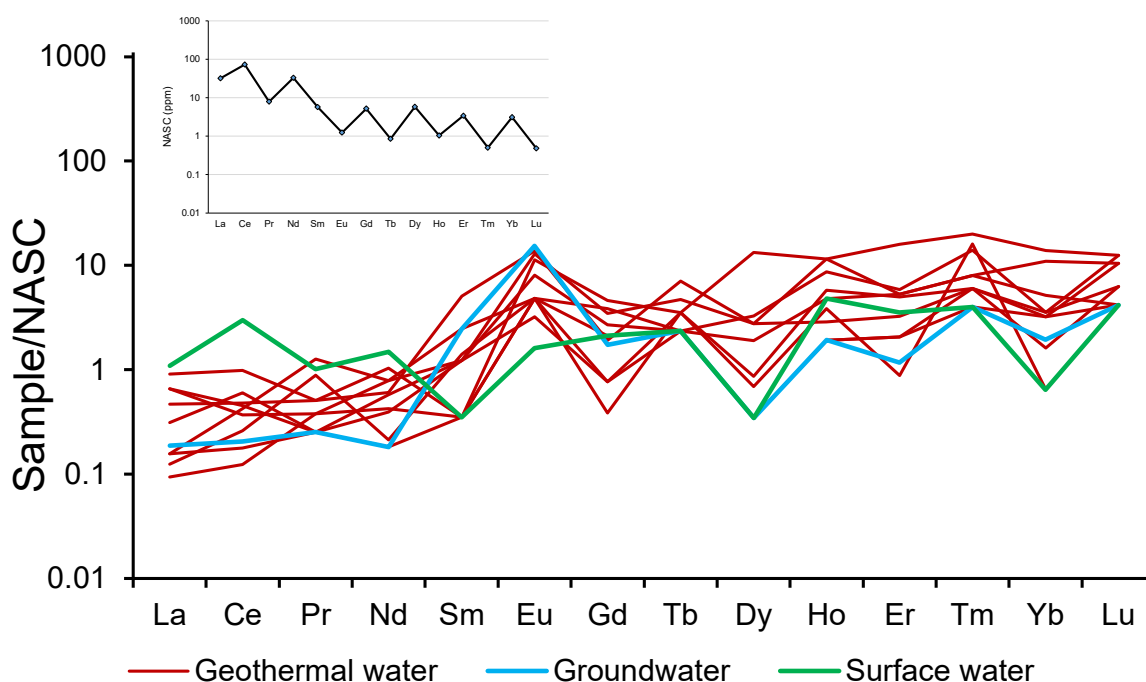

FIGURE 8: NASC-normalized REE patterns for water samples in this study (red, blue and green lines represent geothermal water, groundwater and surface water, respectively)

5.2.2 Origin of dissolved gases

Being dominated by N_2, which is atmospherically only in non-magmatic areas (Arnórsson, 1986), is a typical characteristic of medium-low temperature geothermal systems, suggesting the geothermal fluid had a relative shallow circulation depth with limited contact to deep-derived volatiles (Tian et al., 2021). The nitrogen accumulation is due to its inert activity, while the oxidizing components (such as O_2) were consumed during the long-term interaction between air-saturated water and wall rocks in the reduced runoff. The N_2-He-Ar diagram (Figure 9a) demonstrates that the relative content of these three components is controlled by the mixing between a deep-derived (mantle or crustal) source and the atmospheric endmember. The sample with the highest content of the deep source fluid is from well HZ09 while the sample of well HZ07 has the highest air contribution. The air contamination could have occured either during the sampling procedure or the determination process.

Isotopic helium compositions provide direct information on the origin of the fluid. ^{3}He mainly escapes from the mantle and the predominant source is primordial He that has been trapped within the Earth since the time of its formation, whereas ^{4}He is predominantly produced by the decay of crustal U and Th (O'nions and Oxburgh, 1983). For example, the upper mantle sampled through mid-ocean ridge basalts (MORB) with an R/Ra ratio of 8 is recognized as the typical asthenosphere endmember (Gautheron and Moreira, 2002). The typical ^{3}He/^{4}He ratio of continental crust is in the range of 0.01 – 0.1 with an average of 0.02 (Lupton, 1983). As shown in Figure 9b, all helium in the samples is predominant of crustal origin with around 5% of mantle contribution. Furthermore, accumulation of crustal helium is always accompanied by radiogenic heat of three nuclides, ^{232}Th, ^{235}U and ^{238}U, which are the principal sources of radiogenic heat in the Earth, especially in granites (Waples, 2001, Paternoster et al., 2017). In other words, the radiogenic heat produced by granite rocks could make a big difference in the genesis of geothermal systems in the study area. Indeed, the radiogenic heat rate of the Jurassic granite mass in the study area is 3.15 – 5.78 $\mu W/m^3$, with an average value of 4.39 $\mu W/m^3$ (Kuang et al., 2020a). This value is higher than the average values of both southeast China (4.2 $\mu W/m^3$) (Zhao et al., 1995) and worldwide (2.5 $\mu W/m^3$) (McLaren et al., 2006). Moreover, the granite should be considered as an effective radiogenic heat source when the heat production potential reaches up to 3.1 $\mu W/m^3$ (Paternoster et al., 2017). In addition, the ^{4}He/^{20}Ne ratios show that all samples were contaminated by air by less than 1 % except for HZ02 where the contamination was a little higher than 1%. On the one hand, this phenomenon suggests that the helium isotopic data is reliable without significant air contamination. On the other hand, it indicates that the involvement of excessive O_2 in the gaseous components should be attributed to the contaminantion which occurred during the measurement of gas compositions, rather than to the sampling procedure.
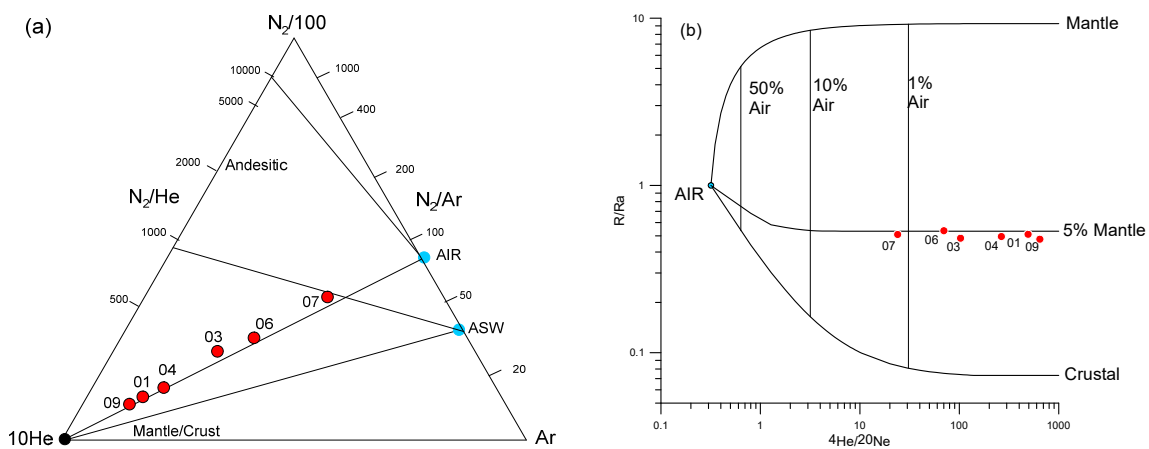

FIGURE 9: (a) Triangle plot of N_2-He-Ar concentrations for dissolved gases from the Huangshadong geothermal field, "AIR" represents the air component with N_2/Ar=84; "ASW" represent the composition of dissolved gas from air saturated groundwater with N_2/Ar=38; (b) He-Ne isotopic compositions (red dots represent geothermal water samples)

5.3 Genesis of the Huangshadong geothermal field and geothermal prospects

Consequently, the underlying Jurassic Monzonitic granite is the reservoir rock and the overlying sedimentary strata, comprising Sinian sandstone, Cambrian sandstone, Devonian clastic rock, Carboniferous sandy shale coal, and Quaternary sand, act as cap rocks for the geothermal system. The geothermal water is recharged by meteoric water without magmatic water or enclosed brine. The infiltrated water circulates down to a depth to 3.5 km. During the long-term deep circulation in the crust, the water was heated to $150 - 165°C$ by the reservoir rocks. Water-rock interactions occurred in the reservoir which resulted in the enrichment of several ions (Na, K, Cl, SO_4, Li, B, F, Rb, etc.) upon dissolution of the diagenetic minerals, such as felspar, silica, muscovite, etc. At the same time, gaseous components of atmospheric origin, such as N_2 and Ar, accumulated due to the inert activity, whereas the oxidizing components (such as O_2) were consumed. In addition, crustal metamorphic products, which include CO_2, CH_4, H_2, ^4He, etc., together with limited amounts of mantle-derived volatiles (^3He, CO_2, etc.) dissolved in the geothermal water. The heated geothermal water rose along the conduit formed by the extensional fracture system. However, the permeability near the surface induced mixing with cold water with ratios of around $25 - 45\%$. Thus, the Huangshadong geothermal system is a medium-temperature geothermal system which is controlled by the deep circulation of geothermal fluid in a fault zone. As proposed by Wilmarth et al. (2020), the power density for a system with reservoir temperature of $150 - 165°C$ could be around 5 MW/km^2.

6. CONCLUSIONS

Based on chemical and isotopic compositions, the evolution process of the geothermal fluid is interpreted, and a conceptual genesis model is proposed for the Huangshadong geothermal area, which is a granite-hosted geothermal system in Southeast China. It is a typical fault control geothermal system in a non-magmatic zone. The reservoir temperature is around 165°C with the geothermal water circulating to a depth of 3.5 km. The geothermal water iss recharged by infiltrating meteoric water and heated by the hot crust. Covered by the sedimentary cap rocks, water-rock interactions occur in the hot granite reservoir. Dissolution of diagenetic minerals, such as feldspar, silica, muscovite, biotite, etc., result in both the accumulation of chemical components (Na, K, Cl, SO_4, Li, B, F, and HREE, etc.) and the enrichment of Sr isotopes in geothermal water. Simultaneously, atmospheric N_2 accumulated in the reductive environment, which is accompanied by deep-derived volatiles (^3He, CO_2) and crustal metamorphic products (^4He, CO_2), dissolving into the geothermal fluid. However, the reservoir temperature and the residence time are still inadequate for the water isotopes showing a positive $\delta^{18}O$ shift. The active extensional fault provides a conduit for the uprising of geothermal fluid. 45% of cold groundwater is mixed into the geothermal fluid due to secondary fractures.

ACKNOWLEDGEMENTS

REFERENCES

Aggarwal, J., Palmer, M., Bullen, T., Arnórsson, S., and Ragnarsdóttir, K., 2000: The boron isotope systematics of Icelandic geothermal waters: 1. Meteoric water charged systems. *Geochimica et Cosmochimica Acta, 64, 4*, 579-585.

Arnórsson, S., 1986: Chemistry of gases associated with geothermal activity and volcanism in Iceland: A review. *Journal of Geophysical Research: Solid Earth, 91, B12*, 12261-12268.

Arnórsson, S., 2000: Mixing processes in upflow zones and mixing models. In: Arnórsson, S. (ed.), *Isotopic and chemical techniques in geothermal exploration, development and use. Sampling methods, data handling, interpretation*. International Atomic Energy Agency, Vienna, 200-211.

Arnórsson, S., Andresdottir, A., Gunnarsson, I., and Stefánsson, A., 1998: New calibration for the quartz and Na/K geothermometers–valid in the range 0-350 C. *Geoscience Society of Iceland Annual Meeting*, 42-43.

Arnórsson, S., Gunnlaugsson, E., and Svavarsson, H., 1983: The chemistry of geothermal waters in Iceland. III. Chemical geothermometry in geothermal investigations. *Geochimica et Cosmochimica Acta, 47, 3*, 567-577.

Byrne, R.H., and Kim, K.H., 1990: Rare earth element scavenging in seawater. *Geochimica Et Cosmochimica Acta, 54, 10*, 2645-2656.

Chen, M., 1992: A new map of hot springs in China and its explanation (in Chinese with English abstract). *Scientia Geologica Sinica, supplementary issue*, 322-332.

Chevychelov, V.Y., Botcharnikov, R., and Holtz, F., 2008: Experimental study of fluorine and chlorine contents in mica (biotite) and their partitioning between mica, phonolite melt, and fluid. *Geochemistry International, 46, 11*, 1081-1089.

Craig, J., Absar, A., Bhat, G., Cadel, G., Hafiz, M., Hakhoo, N., Kashkari, R., Moore, J., Ricchiuto, T., and Thurow, J., 2013: Hot springs and the geothermal energy potential of Jammu & Kashmir State, NW Himalaya, India. *Earth-Science Reviews, 126*, 156-177.

Dupré, B., Gaillardet, J., Rousseau, D., and Allègre, C.J., 1996: Major and trace elements of river-borne material: The Congo Basin. *Geochimica Et Cosmochimica Acta, 60, 8*, 1301-1321.

Gautheron, C. and Moreira, M., 2002: Helium signature of the subcontinental lithospheric mantle. *Earth and Planetary Science Letters, 199, 1-2*, 39-47.

Giggenbach, W.F., 1988: Geothermal solute equilibria. derivation of Na-K-Mg-Ca geoindicators. *Geochimica et cosmochimica acta, 52, 12*, 2749-2765.

He, G., Zhang, H., Xu, Y., and Lu, X., 2017: China's clean power transition: current status and future prospect. *Resources, Conservation Recycling, 121*, 3-10.

Huang, H.Q., Li, X.H., Li, Z.X., and Li, W.X., 2013: Intraplate crustal remelting as the genesis of Jurassic high-K granites in the coastal region of the Guangdong Province, SE China. *Journal of Asian Earth Sciences, 74*, 280-302.

Jiang, G., Hu, S., Shi, Y., Zhang, C., Wang, Z., and Hu, D., 2019: Terrestrial heat flow of continental China: Updated dataset and tectonic implications. *Tectonophysics, 753*, 36-48.

Kuang, J., Wang, S., Qi, S., Xiao, Z., Zhang, M., and Wang, Y., 2020a: Cenozoic tectonic evolution of South China: A brief review, and new insights from the Huangshadong-Shiba area, south-east China.

Geological Journal, 55, 12, 7716-7737.

Kuang, J., Qi, S., Wang, S., Xiao, Z., Zhang, M., Zhao X., and Gan, H., 2020b: Granite intrusion in Huizhou, Guangdong Province and its geothermal implications (in Chinese with English abstract). *Earth Science, 45(4)*, 1461-1480.

Leeman, W. and Sisson, V., 1996: Geochemistry of boron and its implications for crustal and mantle processes. *Boron, 33*, 645-708.

Leyla, B.H., Ren, J., Zhang, J., and Lei, C., 2015: En echelon faults and basin structure in Huizhou Sag, South China Sea: Implications for the tectonics of the SE Asia. *Journal of Earth Science, 26, 5*, 690-699.

Li, J., Pang, Z., Yang, G., Tian, J., Tong, A.L., Zhang, X., and Hu, S., 2017: Million-year-old groundwater revealed by krypton-81 dating in Guanzhong Basin, China. *Science Bulletin, 62, 17,* 1181-1184.

Li, S., Suo, Y., Li, X., Zhou, J., Santosh, M., Wang, P., Wang, G., Guo, L., Yu, S., and Lan, H., 2019: Mesozoic tectono-magmatic response in the East Asian ocean-continent connection zone to subduction of the Paleo-Pacific Plate. *Earth-Science Reviews, 192*, 91-137.

Li, X., 2000: Cretaceous magmatism and lithospheric extension in Southeast China. *Journal of Asian Earth Sciences, 18, 3*, 293-305.

Li, X., Li, Z., He, B., Li, W., Li, Q., Gao, Y., and Wang, X., 2012: The Early Permian active continental margin and crustal growth of the Cathaysia Block: In situ U–Pb, Lu–Hf and O isotope analyses of detrital zircons. *Chemical Geology, 328*, 195-207.

Li, X., Li, Z., Li, W., Liu, Y., Yuan, C., Wei, G., and Qi, C., 2007: U–Pb zircon, geochemical and Sr–Nd–Hf isotopic constraints on age and origin of Jurassic I-and A-type granites from central Guangdong, SE China: a major igneous event in response to foundering of a subducted flat-slab? *Lithos, 96, 1-2*, 186-204.

Ling, H., Shen, W., Sun, T., Jiang, S., Jiang, Y., Ni, P., Gao, J., Huang, G., Ye, H., and Tan, Z., 2006: Genesis and source characteristics of 22 Yanshanian granites in Guangdong province: Study of element and Nd-Sr isotopes. *Acta Petrologica Sinica, 22, 11*, 2687-2703.

Liu, H., Guo, H., Xing, L., Zhan, Y., Li, F., Shao, J., Niu, H., Liang, X., and Li, C., 2016: Geochemical behaviors of rare earth elements in groundwater along a flow path in the North China Plain. *Journal of Asian Earth Sciences, 117*, 33-51.

Lupton, J. E., 1983: Terrestrial inert gases-isotope tracer studies and clues to primordial components in the mantle. *Annual Review of Earth and Planetary Sciences, 11*, 371-414.

McLaren, S., Sandiford, M., Powell, R., Neumann, N., and Woodhead, J., 2006: Palaeozoic intraplate crustal anatexis in the Mount Painter Province, South Australia: timing, thermal budgets and the role of crustal heat production. *Journal of Petrology, 47, 12*, 2281-2302.

Moeller, P., Rosenthal, E., Geyer, S., Guttman, J., Dulski, P., Rybakov, M., Zilberbrand, M., Jahnke, C., and Flexer, A., 2007: Hydrochemical processes in the lower Jordan valley and in the Dead Sea area. *Chemical Geology, 239, 1-2*, 27-49.

O'nions, R. and Oxburgh, E., 1983: Heat and helium in the earth. *Nature, 306, 5942*, 429-431.

Pang, Z., Kong, Y., Li, J., and Tian, J., 2017: An Isotopic Geoindicator in the Hydrological Cycle. *Procedia Earth and Planetary Science, 17*, 534-537.

Parkhurst, D.L. and Appelo, C., 1999: User's guide to PHREEQC (Version 2): A computer program for speciation, batch-reaction, one-dimensional transport, and inverse geochemical calculations. *Water-resources investigations report, 99, 4259*, 312.

Paternoster, M., Oggiano, G., Sinisi, R., Caracausi, A., and Mongelli, G., 2017: Geochemistry of two contrasting deep fluids in the Sardinia microplate (western Mediterranean): Relationships with tectonics and heat sources. *Journal of Volcanology and Geothermal Research, 336*, 108-117.

Riishuus, M., Peate, D., Tegner, C., Wilson, J., and Brooks, C., 2003: Parental magmas to syenitic plutons of the East Greenland volcanic rifted margin: Sr-Nd-Pb isotope evidence from the acid-basic net-veined Astrophyllite Bay complex. *In EGS-AGU-EUG Joint Assembly*, 12820.

Sano, Y., and Wakita, H., 1985: Geographical distribution of 3He/4He ratios in Japan: implications for arc tectonics and incipient magmatism. *Journal of Geophysical Research, 90 B10*, 8729-8741.

Shand, P., Darbyshire, D., Love, A., and Edmunds, W., 2009: Sr isotopes in natural waters: Applications to source characterisation and water–rock interaction in contrasting landscapes. *Applied Geochemistry, 24, 4*, 574-586.

Stober, I. and Bucher, K., 2013: History of geothermal energy use. In: *Geothermal Energy.* Springer, Berlin, Heidelberg, 15-24.

Taylor, S.R. and Mclennan, S.M., 1985: The Continental Crust: Its Composition and Evolution, An Examination of the Geochemical Record Preserved in Sedimentary Rocks. *Blackwell, Oxford*, 312.

Tian, J., Pang, Z., Liao, D., and Zhou, X., 2021: Fluid geochemistry and its implications on the role of deep faults in the genesis of high temperature systems in the eastern edge of the Qinghai Tibet Plateau. *Applied Geochemistry, 131*, 105036.

Wang, J., Hu, S., Pang, Z., He, L., Zhao, P., Zhu, C., Rao, S., Tang, X., Kong, Y., and Luo L., 2012: Estimate of geothermal resources potential for hot dry rock in the continental area of China (in Chinese with English abstract). *Science and Technology Review, 30, 32*, 25-31.

Waples, D. W., 2001: A new model for heat flow in extensional basins: radiogenic heat, asthenospheric heat, and the McKenzie model. *Natural Resources Research, 10, 3*, 227-238.

Xia, L. and Zhang, Y., 2019: An overview of world geothermal power generation and a case study on China—The resource and market perspective. *Renewable and Sustainable Energy Reviews, 112*, 411-423.

Xiao, Z., Wang, S., Qi, S., Kuang, J., Zhang, M., Tian, F., and Han, Y., 2020: Petrogenesis, Tectonic Evolution and Geothermal Implications of Mesozoic Granites in the Huangshadong Geothermal Field, South China. *Journal of Earth Science, 31, 1*, 141-158.

Yan, X., Gan, H., and Yue, G., 2019: Hydrogeochemical characteristics and genesis of typical geothermal fields from Huangshadong to Conghua in Guangdong (in Chinese with English abstract). *Geological Review, 65, 3*, 225-236.

Zhang, J., Zhao, Z., Yan, Y., Cui, L., Wang, Q., Meng, J., Li, X., and Liu, C., 2021: Lithium and its isotopes behavior during incipient weathering of granite in the eastern Tibetan Plateau, China. *Chemical Geology, 559*, 119969.

Zhao, K., Jiang, S., Nakamura, E., Moriguti, T., Palmer, M.R., Yang, S., Dai, B., and Jiang, Y., 2011: Fluid–rock interaction in the Qitianling granite and associated tin deposits, South China: evidence from boron and oxygen isotopes. *Ore Geology Reviews, 43, 1*, 243-248.

Zhao, P, Wang, J., Wang, J., and Luo, D., 1995: Characteristics of heat production distribution in SE China (in Chinese with English abstract). *Acta Petrologica Sinica, 11, 3*, 292-305.

Zhong, T. and Zhou, D., 1990: A preliminary study of the relationship between the distribution of hot springs and the activity of earthquakes along South China Coast (in Chinese with English abstract). *South China Seismology Journal, 10, 4*, 22-29.

Zhou, X. and Li, W., 2000: Origin of Late Mesozoic igneous rocks in Southeastern China: implications for lithosphere subduction and underplating of mafic magmas. *Tectonophysics, 326, 3-4*, 269-287.

Zhu, W., Zhong, H., Li, X., He, D., Song, X., Ren, T., Chen, Z., Sun, H, and Liao, J., 2010: The early Jurassic mafic–ultramafic intrusion and A-type granite from northeastern Guangdong, SE China: age, origin, and tectonic significance. *Lithos, 119, 3-4*, 313-329.

APPENDIX I: Information about sampling sites, field test parameters and major component concentrations (units of the columns without marks are in mg/L; "TW" represents thermal groundwater well; "GW" represents cold groundwater well; "SW" represents surface water from the Huangshadong reservoir; "C.B." means charge balance; "-" represents under detection limit; "n.a." represents not analysed)

No.	HZ01	HZ02	HZ03	HZ04	HZ05	HZ06	HZ07	HZ08	HZ09	HZ10	HZ11
Type	TW	TW	TW	TW	TW	TW	TW	TW	TW	GW	SW
Depth (m)	280	200	360	190	150	300	350	400	350	20	0
T (°C)	55	99	48	52	49	50	52	50	50	32	19
pH	7.49	7.88	7.82	7.66	8.32	7.13	8.15	7.49	7.12	6.77	7.89
EC (µs/cm)	1259	1721	1024	1210	1293	479	1431	1608	1513	274	22.5
TDS	532	727	398	473	496	192	554	633	591	118	11
S^{2-} (µg/L)	24	111	10	2	9	26	29	58	41	16	8
Fe^{2+}	0.31	0.04	0.02	0.8	0.12	0.44	0.69	0.53	0.49	0.04	-
Na^+	203	240	176.8	194.2	202	47.8	228.1	203	180.7	41.7	2.1
K^+	16.2	18.3	7	12	12.7	4.3	13.3	15.2	14.3	3.7	0.9
Mg^{2+}	1.8	0.4	1.4	1.1	1.2	2.6	2.2	5.5	1.4	4	0.7
Ca^{2+}	41.6	12.7	19.1	22.4	24.4	24.6	40.6	23.9	34.3	6.5	1.7
Cl^-	51.2	58.5	21.2	29.2	31.5	5.9	30.1	25.4	32.5	7.6	2.2
SO_4^{2-}	88.3	111.7	41.4	55.8	61.9	13	61.5	54.6	58	10.8	3.8
HCO_3^-	544	554	448.9	457.7	452.7	178.8	545.2	632.8	534	110	9.5
F^-	8.7	14.3	6.7	11.3	10.6	6.6	8.7	9.3	8.8	1.9	0.2
SiO_2	119.1	186.9	77.9	121.7	148.3	91.7	77.9	33.7	60.4	12	10.4
C.B. (%)	-3.09	-6.01	0.71	2.44	4.13	3.71	5.96	-5.9	-3.97	6.67	-7.61
$\delta^{18}O$ (‰)	-7.6	-7.3	-7.6	-7.6	-7.5	-7.5	-7.4	-7.8	-7.4	-7.2	-3.9
δ^2H (‰)	-45.5	-45.0	-46.0	-45.1	-44.9	-44.9	-44.2	-46.2	-44.3	-42.2	-28.6
$^{87}Sr/^{86}Sr$	0.728	0.720	0.731	0.727	0.727	0.734	0.729	0.729	0.728	0.733	0.725

APPENDIX II: Chemical and isotopic compositions of the dissolved gas samples
(R is the $^3He/^4He$ ratio of sample and Ra is the $^3He/^4He$ ratio of air, 1.41×10^{-6})

No.	Chemical composition (vol. %)							Isotopic ratios		
	H_2	He	CH_4	N_2	O_2	Ar	CO_2	$^3He/^4He$	$^4He/^{20}Ne$	R/Ra
HZ01	0.1700	0.3714	1.58	82.19	4.28	0.92	10.27	7.20E-07	492	0.51
HZ03	0.2600	0.1343	0.11	83.55	11.43	0.8500	3.60	6.82E-07	103	0.48
HZ04	0.1300	0.3081	1.14	83.89	4.26	0.99	9.12	6.98E-07	265	0.50
HZ06	0.0002	0.1313	0.64	94.13	3.10	1.06	0.89	7.56E-07	70	0.54
HZ07	0.0140	0.0442	0.04	76.81	16.98	0.85	5.26	7.18E-07	24	0.51
HZ09	0.0003	0.5587	0.32	90.46	0.24	1.02	7.13	6.73E-07	646	0.48

APPENDIX III: Trace element concentrations (µg/L)

No.	Br	Al	Li	B	As	Be	Sc	Ti	Cu	Rb	Cs	W	Ba	Mn	Sr	Zn
HZ01	82.5	11.4	1373.0	586.0	<0.6	5.3	30.2	15.6	3.8	253.0	137.0	63.0	129.0	380.0	361.0	19.5
HZ02	100.9	29.7	1544.0	621.0	1.3	5.5	42.0	18.3	3.5	277.0	170.0	127.0	50.3	103.0	286.0	9.5
HZ03	47.2	20.8	698.0	315.0	<0.6	1.6	14.9	8.3	1.8	68.1	37.6	19.0	42.6	73.9	243.0	8.7
HZ04	62.8	31.5	818.0	383.0	0.8	6.0	25.7	12.5	2.1	165.0	112.0	75.9	49.5	174.0	136.0	5.2
HZ05	63.2	20.5	855.0	416.0	1.0	7.3	24.9	14.6	2.1	162.0	124.0	98.4	73.5	186.0	135.0	13.1
HZ06	20.2	11.0	132.0	56.6	<0.6	1.1	14.8	6.9	0.8	27.5	15.7	14.2	68.6	214.0	113.0	13.4
HZ07	61.7	31.4	972.0	487.0	<0.6	2.3	15.8	8.0	2.3	139.0	63.8	52.5	127.0	197.0	473.0	6.0
HZ08	58.9	21.4	1140.0	645.0	<0.6	2.3	6.5	4.6	2.6	122.0	41.5	51.3	101.0	75.1	596.0	6.5
HZ09	57.4	15.1	1046.0	478.0	<0.6	2.6	14.0	7.9	2.8	194.0	104.0	55.3	117.0	204.0	330.0	11.7
HZ10	34.9	27.2	82.8	106.0	<0.6	0.2	9.8	5.4	2.5	3.4	0.2	2.6	66.2	2.6	41.8	19.6
HZ11	11.1	10.6	1.2	6.7	0.7	0.0	3.3	0.8	1.0	2.9	0.1	0.1	3.4	2.6	6.8	4.2

No.	La	Ce	Pr	Nd	Sm	Eu	Gd	Tb	Dy	Ho	Er	Tm	Yb	Lu	δEu	δCe
HZ01	0.029	0.072	0.004	0.034	<0.002	0.014	0.024	0.003	0.077	0.012	0.054	0.01	0.043	0.006	4.55	1.40
HZ02	0.004	0.019	0.007	0.007	0.008	0.006	0.02	0.002	0.019	0.009	0.02	0.007	0.011	0.006	1.84	0.51
HZ03	0.003	0.009	0.003	0.014	<0.002	0.006	0.011	<0.002	<0.002	<0.002	0.007	0.003	0.005	0.003	3.92	0.52
HZ04	0.015	0.035	0.004	0.02	0.029	0.017	0.01	0.006	0.016	0.012	0.018	0.004	0.034	0.005	3.91	0.98
HZ05	0.005	0.031	0.01	0.026	0.014	0.006	0.004	0.003	0.004	0.004	0.003	0.008	<0.002	<0.002	3.00	0.60
HZ06	0.021	0.027	0.003	0.026	0.007	0.004	0.004	<0.002	<0.002	<0.002	0.007	<0.002	0.01	0.005	3.23	0.71
HZ07	0.01	0.044	0.002	0.013	0.007	0.016	0.018	0.004	0.016	0.003	0.011	0.003	0.011	0.003	5.50	2.13
HZ08	0.005	0.013	<0.002	0.006	<0.002	0.006	<0.002	0.003	0.005	0.006	0.017	0.003	0.01	<0.002	13.16	0.87
HZ09	0.021	0.033	0.002	0.019	0.007	0.01	0.014	<0.002	0.011	0.005	0.018	0.004	0.016	<0.002	4.11	0.99
HZ10	0.006	0.015	<0.002	0.006	0.014	0.019	0.009	<0.002	<0.002	<0.002	0.004	<0.002	0.006	<0.002	7.32	0.93
HZ11	0.035	0.217	0.008	0.049	<0.002	<0.002	0.011	<0.002	<0.002	0.005	0.012	<0.002	<0.002	<0.002	1.31	2.82

$\delta Ce = Ce/Ce^* = Ce_N/(La_N * Pr_N)^{0.5} \approx 2Ce/(La_N + Pr_N)$; $\delta Eu = Eu/Eu^* = Eu_N/(Sm_N * Gd_N)^{0.5} \approx 2Ce/(Sm_N + Gd_N)$ (Moeller et al., 2007)

APPENDIX IV: Correlation matrix for ions in water samples from the study area

	Na⁺	K⁺	Mg²⁺	Ca²⁺	Cl⁻	SO₄²⁻	HCO₃⁻	F⁻	SiO₂	S²⁻	Fe²⁺	Br	Al	Li	B	As	Be	Sc	Ti	Cu	Rb	Cs	W	Ba	Mn	Sr
Na⁺	1.00																									
K⁺	0.92	1.00																								
Mg²⁺	-0.12	-0.05	1.00																							
Ca²⁺	0.61	0.60	0.05	1.00																						
Cl⁻	0.85	0.92	-0.32	0.48	1.00																					
SO₄²⁻	0.89	0.94	-0.29	0.47	0.99	1.00																				
HCO₃⁻	0.96	0.93	0.05	0.68	0.80	0.83	1.00																			
F⁻	0.88	0.88	-0.21	0.47	0.83	0.87	0.83	1.00																		
SiO₂	0.64	0.63	-0.54	0.28	0.76	0.77	0.50	0.84	1.00																	
S²⁻	0.42	0.60	0.03	-0.01	0.59	0.63	0.45	0.55	0.39	1.00																
Fe²⁺	0.36	0.36	0.23	0.63	0.11	0.14	0.44	0.37	0.04	-0.09	1.00															
Br	0.89	0.93	-0.20	0.43	0.98	0.98	0.83	0.86	0.74	0.60	0.14	1.00														
Al	0.48	0.33	0.05	-0.05	0.29	0.34	0.34	0.43	0.27	0.23	0.26	0.45	1.00													
Li	0.93	0.98	-0.13	0.56	0.95	0.97	0.93	0.85	0.63	0.61	0.24	0.95	0.29	1.00												
B	0.93	0.97	0.06	0.58	0.87	0.90	0.96	0.81	0.50	0.57	0.32	0.90	0.33	0.97	1.00											
As	0.18	0.21	-0.61	-0.42	0.34	0.37	0.00	0.41	0.61	0.29	-0.27	0.35	0.29	0.20	0.10	1.00										
Be	0.72	0.72	-0.39	0.36	0.76	0.76	0.60	0.81	0.85	0.17	0.18	0.77	0.28	0.68	0.62	0.59	1.00									
Sc	0.62	0.66	-0.52	0.24	0.85	0.83	0.48	0.78	0.94	0.47	-0.03	0.83	0.32	0.68	0.54	0.57	0.81	1.00								
Ti	0.69	0.71	-0.45	0.34	0.86	0.85	0.57	0.81	0.94	0.37	0.00	0.86	0.30	0.72	0.60	0.51	0.88	0.97	1.00							
Cu	0.67	0.81	0.03	0.39	0.86	0.82	0.67	0.54	0.40	0.54	0.03	0.87	0.28	0.82	0.80	0.06	0.50	0.60	0.64	1.00						
Rb	0.84	0.94	-0.34	0.54	0.98	0.97	0.80	0.85	0.75	0.55	0.23	0.94	0.22	0.94	0.87	0.35	0.80	0.82	0.84	0.81	1.00					
Cs	0.78	0.85	-0.49	0.42	0.94	0.92	0.69	0.86	0.86	0.45	0.14	0.90	0.25	0.85	0.75	0.53	0.90	0.89	0.92	0.71	0.96	1.00				
W	0.80	0.86	-0.36	0.30	0.87	0.90	0.70	0.92	0.86	0.56	0.15	0.88	0.42	0.82	0.76	0.65	0.89	0.84	0.86	0.61	0.89	0.93	1.00			
Ba	0.53	0.61	0.37	0.88	0.44	0.43	0.63	0.35	0.08	0.16	0.53	0.44	0.02	0.54	0.61	-0.53	0.21	0.12	0.23	0.56	0.48	0.32	0.23	1.00		
Mn	0.45	0.53	-0.19	0.86	0.54	0.50	0.47	0.47	0.51	-0.05	0.45	0.44	-0.25	0.50	0.43	-0.17	0.54	0.49	0.56	0.38	0.61	0.57	0.37	0.68	1.00	
Sr	0.71	0.72	0.41	0.65	0.51	0.56	0.83	0.50	0.07	0.47	0.46	0.54	0.18	0.73	0.82	-0.35	0.14	0.07	0.13	0.53	0.50	0.28	0.33	0.72	0.32	1.00